Triferroic coupling in two-dimensional $WRuCl_6$

Shiqiang Yu, Dongyue Sun, Yushuo Xu, Ying Dai,* Baibiao Huang, and Wei Wei†

School of Physics, State Key Laboratory of Crystal Materials, Shandong University, Jinan 250100, China

(Received 22 January 2024; revised 7 July 2024; accepted 26 July 2024; published 14 August 2024)

In this work, we report that electrically controlled ferroic properties and multistate storage can be achieved in dual-metal trihalide $WRuCl_6$ monolayer from the perspectives of first-principles calculations. We confirm that it is a rare two-dimensional (2D) triferroics, and, particularly, ferromagnetism and ferroelasticity are coupled strongly to the ferroelectricity of 120° rotation symmetry. It therefore can enable the flexible and reversible switching of ferroic orders via electric field. In addition, $WRuCl_6$ monolayer is an intrinsic bipolar magnetic semiconductor; thus, the switchable spin-polarized carrier can be obtained by applying an electric gate voltage. Therefore, it provides an extra parameter to further improve the storage density. Our work not only offers a paradigm for the multiferroic coupling physics, but also provides a promising platform for multistate storage and multifunctional nanodevices.

DOI: 10.1103/PhysRevB.110.064417

I. INTRODUCTION

Because of the exponential growth of data, seeking new materials suitable for high-density multistate storage becomes increasingly vital. In this context, two-dimensional (2D) multiferroic materials as ideal platforms meeting the escalating storage needs have been attracting extensive attention [1,2]. In particular, 2D triferroics with three types of ferroic orders (ferromagnetism, ferroelectricity, and ferroelasticity) imply great significance not only in fundamental multiferroic physics but also in emerging applications. The multiferroic coupling in triferroics endows the materials multiple stimuli-responsive properties, enabling simultaneous switching of different ferroic orders by external stress, magnetic field, or more convenient electric field [3–5]. Therefore, 2D triferroic materials with fascinating multiferroic coupling can be anticipated to develop innovative nanodevices in fields of information storage, as well as spintronics and quantum technology.

Up to now, triferroics has primarily been discussed in three-dimensional systems [6–8]. However, intrinsic triferroics in 2D case is extremely rare [9–11], and there are drawbacks in practical applications. For instance, unfavorable antiferromagnetic (AFM) state remains unchanged during the ferroic order switching, imposing limitations in the information processing [9,10]. In addition, the data storage density is low in materials with strong multiferroic coupling; on the other hand, the possibility of the long-sought tunable ferroic properties through an external electric field will be prohibited in materials with weak multiferroic coupling [11]. The solution to address this dilemma has not yet been reported. In this context, going beyond the existing paradigm, a new approach that allows the coexistence of multiferroic coupling and multiple storage states in 2D triferroics is of significant importance. Especially, intrinsic ferromagnetic (FM) 2D triferroics is more interesting.

In this work, we demonstrate an approach to accommodate the multiferroic coupling and multistate storage. We assume that the flexible and reversible switching of FM and ferroelastic (FA) orders can be realized through the mediation of ferroelectric (FE) order. We confirm its feasibility in the $WRuCl_6$ monolayer, an extremely rare case of 2D triferroics. In $WRuCl_6$ monolayer, 120° rotation-symmetry ferroelectricity, ferromagnetism, and ferroelasticity coexist, and there is a robust coupling between the FM, FA, and FE orders. This ensures the external electric field-mediated switching of the other two ferroic states. In addition, $WRuCl_6$ monolayer is an intrinsic bipolar magnetic semiconductor with adjustable Fermi level under electric gate voltage and switchable spin-polarized carriers, which can be utilized as an effective signal to enhance the storage capacity. Therefore, the triferroic $WRuCl_6$ monolayer provides an appealing platform for cutting-edge information technology.

II. COMPUTATIONAL METHODS

In the present work, the first-principles calculations based on density-functional theory were performed employing the projector augmented-wave method, as implemented in the Vienna *Ab initio* Simulation Package (VASP) [12,13]. The exchange-correlation functional was described by the Perdew-Burke-Ernzerhof form of the generalized gradient approximation (GGA) [14]. In accordance to the GGA+U strategy used in previous works, $U = 1$ eV was considered for W element [15,16], and the relevant test data are presented in subsequent sections. A Γ-centered Monkhorst-Pack k-point mesh of $9 \times 9 \times 1$ was employed [17]. The energy cutoff was set to 520 eV, and a vacuum space of more than 15 Å was used for eliminating the interactions between periodic slabs. Structure optimization would stop after the energy was

*Contact author: daiy60@sdu.edu.cn

†Contact author: weiw@sdu.edu.cn

smaller than 10^{-6} eV and the residual force on each atom was less than -0.01 eV/Å. The phonon-dispersion spectrum was calculated based on the density-functional perturbation theory by using the PHONOPY code to confirm the dynamical stability [18], and the thermal stability was addressed at 300 K through *ab initio* molecular dynamics (AIMD) calculations. In addition, climbing image nudged elastic band (CINEB) method was used to search for the ferroelectric switching pathway with minimum energy barrier [19]. In order to evaluate the experimental feasibility, cohesive energy E_{coh} was also calculated:

$$E_{\mathrm{coh}} = \frac{E_{\mathrm{WRuCl_6}} - E_{\mathrm{W}} - E_{\mathrm{Ru}} - 6E_{\mathrm{Cl}}}{8},$$

where $E_{\mathrm{WRuCl_6}}$, E_{W}, E_{Ru}, and E_{Cl} are the total energies of the $WRuCl_6$ monolayer, and single W, Ru, and Cl atoms, respectively. Based on the Heisenberg spin Hamiltonian model, Monte Carlo (MC) simulations were performed based on a $16 \times 16 \times 1$ supercell to evaluate the Curie temperature T_c. In addition, specific-heat capacity C_v was estimated, which is defined as [20]

$$C_v = \frac{\langle E^2 \rangle - \langle E \rangle^2}{k_B T^2}.$$

In particular, 10^6 simulation steps were calculated after the system reached equilibrium state, as parametrized in the MCSOLVER distribution [21–23].

III. RESULTS AND DISCUSSION

In the case for geometric ferroelectrics, electric polarization originates from the displacement of opposite charge centers caused by spontaneous structural distortion. The direction of electric polarization can be switched by changing the structural distortion direction. According to our assumption, the FE phase transition should be accompanied by the switching of other ferro-related properties. Specifically, the response of the electric polarization of FE structures to an external electric field can lead to FE phase transition, and, simultaneously, result in the switching of magnetic and FA order. In such a way, experimentally feasible nonvolatile electrically controlled ferromagnetism and ferroelasticity can be realized with low energy consumption, and the potential ways for multistate storage can be further discussed.

In the 2D material family, transition-metal trihalide of hexagonal lattice, i.e., MX_3 ($X =$ Cl, Br, and I), has been gaining extensive attention due to its unique electronic properties [24,25]. In particular, MX_3 monolayers can be easily exfoliated from their van der Waals bulk phases and most of them exhibit intrinsic magnetism. Because of their inversion or rotational symmetry, nevertheless, spontaneous electric polarization is absent [26–28]. In accordance to the mechanism, the candidates in 2D limit should be featured by ferroelectricity and robust magnetoelectric coupling; thus, MX_3 is excluded from realizing the electrically controlled ferromagnetism and ferroelasticity. It is of high interest that the inversion symmetry and rotational symmetry (C_3) can be broken in the heteronuclear dual transition-metal trihalide $M1M2X_6$ monolayers, which originate from the parent MX_3 structure

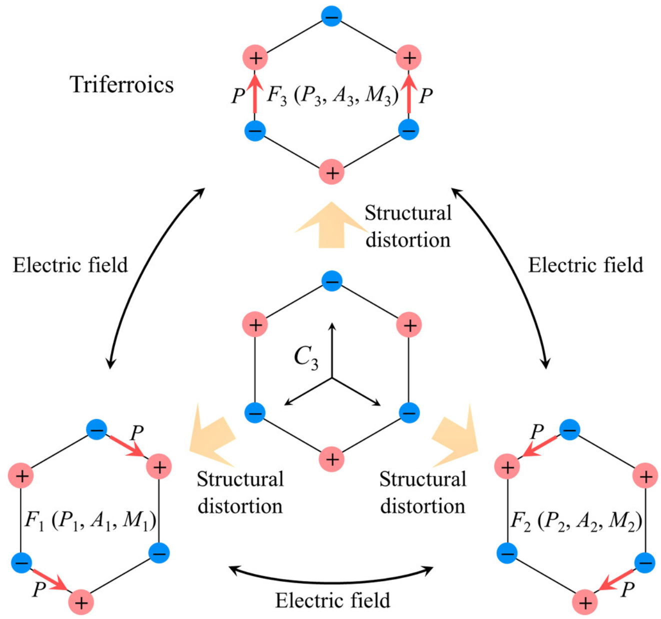

FIG. 1. Schematic of electrically controlled ferroic properties in heteronuclear dual transition-metal trihalide monolayer. Red and blue dots represent positively and negatively charged ions, respectively, and red arrows stand for electric polarization.

($M =$ Ti, V, Cr, Mn, Fe, Co, Ru, W, Re, etc.; and $X =$ Cl, Br, I). In this case, electric polarization arises, and, therefore, $M1M2X_6$ monolayers can probably follow the mechanism. In the $M1M2X_6$ monolayers, dimerization occurs for neighboring metal ions due to the Jahn-Teller effect, giving rise to the spontaneous structural distortion and resulting in an electric polarization along the dimerization [16]. It should be emphasized that in such 2D lattices, interestingly, three energetically equivalent FE states of 120° rotation symmetry will emerge, enabling higher storage density compared to the conventional ferroelectrics. In addition, it can be observed from the structural features that these FE states correspond actually to three orientation variants, i.e., FA states. In T'-phase MX_2 with a distorted hexagonal lattice, such a ferroelasticity induced by spontaneous structural distortion has also been confirmed [29]. In case the easy-magnetization axis is also switchable with the FE/FA state, as demonstrated in Fig. 1, the desired electrical control of ferromagnetism and ferroelasticity can therefore be expected in $M1M2X_6$ monolayers.

In the following, we will verify this approach in a representative dual transition-metal trihalide monolayer, $WRuCl_6$. In Fig. 2(a), the crystal structure of $WRuCl_6$ monolayer (in F_1 state) with a point-group symmetry of C_2 is presented. It can be observed that each metal ion is located at the center of a distorted octahedron, bonding to six Cl ions. The nearest-neighbor (NN) W and Ru atoms tend to form W–Ru dimer, which is attributed to the Jahn–Teller effect, with a bond length a_1 of 2.88 Å shorter than other two W–Ru bonds of 3.68 Å (a_2 and a_3). In Table S1 and Fig. S1 [30], the thermodynamic, mechanical, thermal, and dynamical stability of $WRuCl_6$ monolayer is verified by cohesive energy, elastic constants, AIMD simulations, and phonon band dispersion,

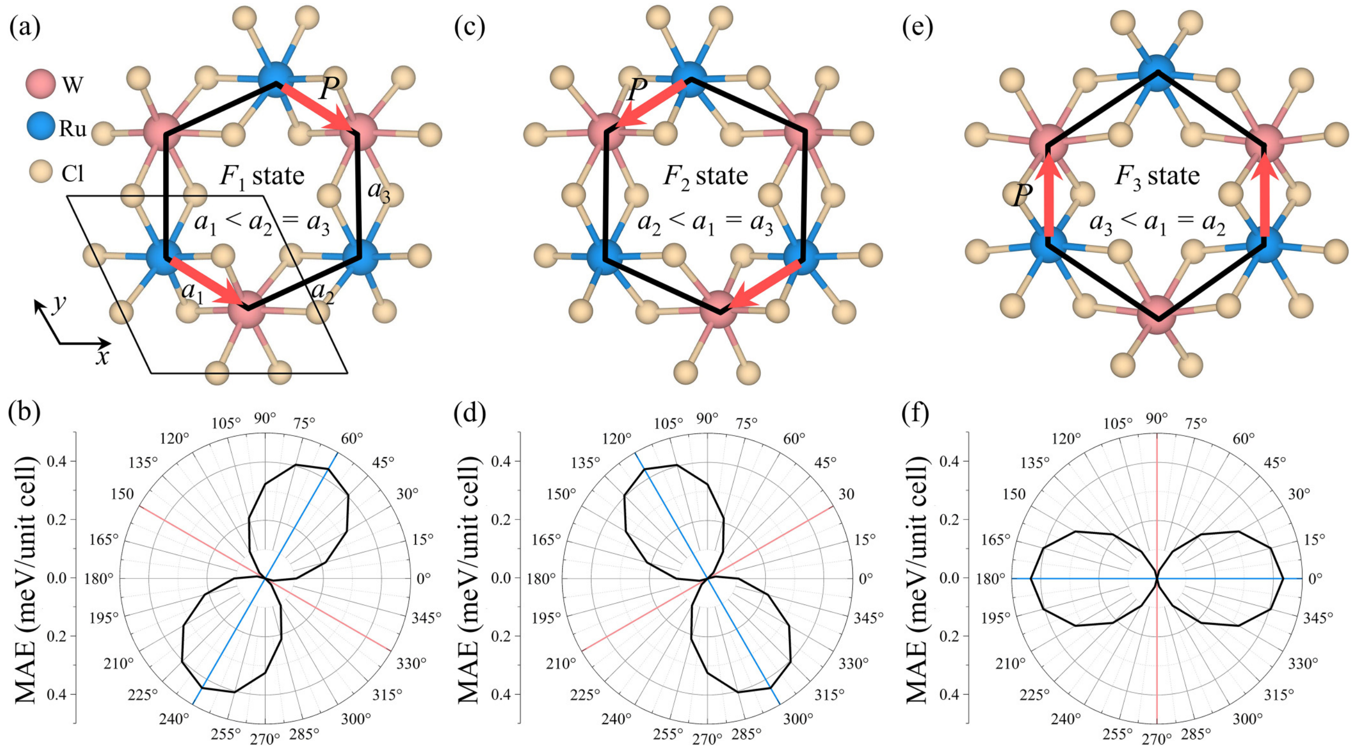

FIG. 2. Top view of $WRuCl_6$ monolayer of (a) F_1, (c) F_2, and (e) F_3 states. Red, blue, and yellow spheres represent W, Ru, and Cl atoms, respectively. a_1, a_2, and a_3 characterize distorted hexagonal lattice in three states. Magnetic anisotropy energy (MAE) for $WRuCl_6$ monolayer of (b) F_1, (d) F_2, and (f) F_3 states. Energy of spin direction along easy-magnetization axis is taken as the reference. Red and blue lines represent spin directions corresponding to the minimum and maximum energies, respectively.

respectively. The results strongly suggest that $WRuCl_6$ monolayer is experimentally feasible.

It has already been known that distorted octahedral crystal field can categorize metal d orbitals into two groups, namely, t_{2g} ($1a$, $1e_x$, $1e_y$) and e_g ($2e_x$, $2e_y$) states [31,32]:

$$1a \equiv r^2$$

$$1e_x \equiv \sqrt{\frac{2}{3}}d_{xy} - \sqrt{\frac{1}{3}}d_{xz},$$

$$1e_y \equiv \sqrt{\frac{2}{3}}d_{x^2-y^2} - \sqrt{\frac{1}{3}}d_{yz},$$

$$2e_x \equiv \sqrt{\frac{1}{3}}d_{xy} + \sqrt{\frac{2}{3}}d_{xz},$$

$$2e_y \equiv \sqrt{\frac{1}{3}}d_{x^2-y^2} + \sqrt{\frac{2}{3}}d_{yz}.$$

In line with Hund's rules and Pauli exclusion principle, the six valence electrons of Ru ion will fully fill the lower t_{2g} states, while the two valence electrons of W ion will partly occupy the t_{2g} states; see Fig. S2 [30]. It therefore gives rise to formal magnetic moments of 2 and 0 μ_B for W and Ru ions, respectively, which are consistent with the results from first principles (1.808 μ_B for W ion and 0.017 μ_B for Ru ion).

In an alternative way, we recalculate the density of states (DOS) to straightforwardly explain the origin of the magnetic moment of $WRuCl_6$ monolayer, see the results in Fig. 3. In particular, the lattice of the unit cell of the material is appropriately rotated, so that the z-axis is aligned with the W–Cl bond. In this case, $W - 5d$ orbitals under a distorted octahedral crystal field are categorized into (d_{xy}, d_{xz} and d_{yz}) and ($d_{x^2-y^2}$ and d_{z^2}) groups, as the common case usually discussed in literatures. It can be seen from the projected DOS that the band-edge states of $WRuCl_6$ monolayer are mainly

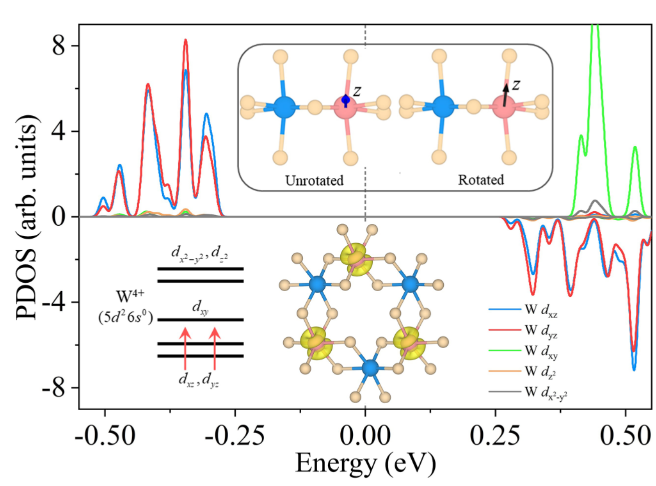

FIG. 3. Orbital-projected density of states (PDOS) for $WRuCl_6$ monolayer with FM F_1 state. Insets show the rotated and unrotated structure, W 5d orbital splitting, and spin charge density of $WRuCl_6$ monolayer; the maximum electronic density is 0.03 e Å^{-3}.

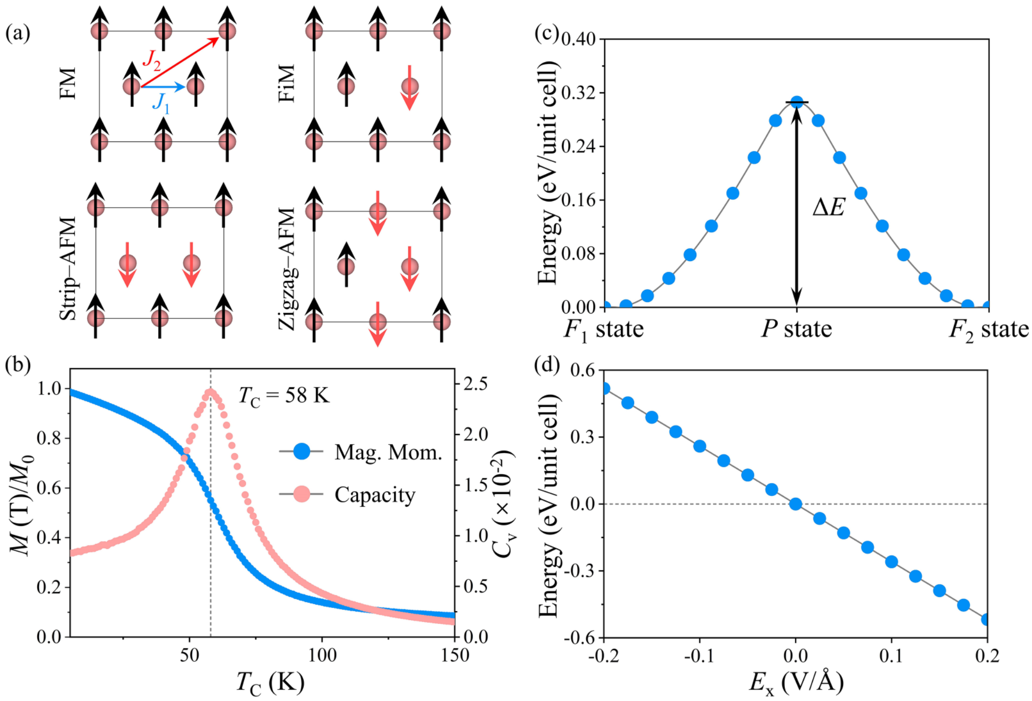

FIG. 4. (a) FM, FiM, stripe AFM, and zigzag AFM orders considered for $WRuCl_6$ monolayer. (b) Normalized magnetization and specific heat as a function of temperature. (c) Energy distribution of $WRuCl_6$ monolayer for F_1-to-F_2 phase transition. (d) Energy difference between F_1 and F_2 states under x-direction external electric field.

contributed by W atom. In particular, d_{xz} and d_{yz} orbitals remain degenerate while the energy of d_{xy} orbital is elevated, confirming the magnetic moment of 2 μ_B for W atom. In addition, spin charge-density distribution based on the reconstructed lattice is also shown as an inset to Fig. 3, suggesting identical results to those attained from the original lattice. In Fig. S3 [30], the local magnetic moments of W and Ru atoms with different U_{eff} values are shown. It can be found that W and Ru atoms remain the magnetic moments of formally 2 and 0 μ_B, respectively, indicative of the robustness against the variation of U_{eff}.

In order to identify the magnetic ground state of $WRuCl_6$ monolayer, FM, ferrimagnetic (FiM), stripy-AFM, and zigzag-AFM orders are taken into account; see Fig. 4(a). In addition, for these magnetic orders of consideration, both in-plane and out-of-plane spin directions are included. In accordance with our results summarized in Table S2 [30], the in-plane FM order turns out to be the magnetic ground state. In particular, $WRuCl_6/MoS_2$ heterobilayer is considered to examine the stability of the magnetic state of $WRuCl_6$ monolayer; see Fig. S4 [30]. In order to minimize the lattice mismatch, a unit cell of $WRuCl_6$ and a $\sqrt{3}\times\sqrt{3}$ supercell of MoS_2 are combined to construct the bilayer, and the in-plane lattice parameter is fixed to that of $WRuCl_6$ monolayer with a lattice mismatch of 4.64%. In Table S3 [30], total energy reveals that the substrate effect is slight, and the magnetic ground state of $WRuCl_6$ monolayer retains the in-plane FM order.

In Fig. 2(b), in-plane magnetic anisotropy energy (MAE) is shown with the lowest total energy set to zero. It is obvious that the total energy presents a strong dependence on the direction of magnetization, indicating a robust coupling with the rotation angle. It can be found that the easy-magnetization axis is along the [–110]/[1–10] direction, with the energies of 0.11, 0.43, and 0.60 meV per unit cell lower than that along [100], [110], and [001] (z axis) directions, respectively. It should be emphasized that the restriction of Mermin-Wagner theorem is broken in $WRuCl_6$ monolayer through such an in-plane anisotropic magnetization [33,34], ensuring the long-range FM order. It is of interest to see that the direction of the easy magnetization is parallel/antiparallel to the direction of the in-plane electric polarization, implicating the potential of electrically controlled magnetism.

In order to describe the magnetic behavior of $WRuCl_6$ monolayer, a Heisenberg spin Hamiltonian model is employed:

$$H = H_0 - J_1 \sum_{\langle ij\rangle} \boldsymbol{S}_i \boldsymbol{S}_j - J_2 \sum_{\langle mn\rangle} \boldsymbol{S}_m \boldsymbol{S}_n - \lambda \sum_{\langle ij\rangle} \boldsymbol{S}_i^z \boldsymbol{S}_j^z - A \sum_i \left(\boldsymbol{S}_i^z\right)^2 - \sum_{\langle ij\rangle} \boldsymbol{D}_{ij}(\boldsymbol{S}_i \times \boldsymbol{S}_j).$$

Here, J_1 and J_2 stand for the NN, next-nearest neighbor (NNN) exchange interaction, respectively; $\langle ij\rangle$ and $\langle mn\rangle$ correspond to the NN and NNN magnetic atoms; $\boldsymbol{S}$ is spin operator; A, λ, and D_{ij} represent the coefficient of single-ion anisotropy, Heisenberg anisotropic symmetric exchange, and Dzyaloshinskii-Moriya interaction (DMI), respectively; and $\boldsymbol{S}_{i,j}^z$ symbolizes the component of $\boldsymbol{S}_i$ along the z axis. In Table S2 [30], the total energies of different magnetic configurations are summarized, according to which the magnetic interaction parameters J_1, J_2, λ, A, and D_{ij} can be determined:

$$\begin{aligned}
E_{\mathrm{FM}-x} &= E_0 - 12J_1 - 12J_2,\\
E_{\mathrm{FM}-z} &= E_0 - 12J_1 - 12J_2 - 12\lambda - 4A,\\
E_{\mathrm{stripy-AFM-x}} &= E_0 + 4J_1 + 4J_2,\\
E_{\mathrm{stripy-AFM}-z} &= E_0 + 4J_1 + 4J_2 + 4\lambda - 4A,\\
E_{\mathrm{zigzag-AFM}-x} &= E_0 + 4J_1 - 4J_2,\\
E_{\mathrm{zigzag-AFM}-z} &= E_0 + 4J_1 - 4J_2 + 4\lambda - 4A,\\
J_1 &= \frac{2E_{\mathrm{zigzag-AFM}-x} - E_{\mathrm{FM}-x} - E_{\mathrm{stripy-AFM}-x}}{16},\\
J_2 &= \frac{E_{\mathrm{stripy-AFM}-x} - E_{\mathrm{zigzag-AFM}-x}}{8},\\
\lambda &= \frac{E_{\mathrm{stripy-AFM}-z} + E_{\mathrm{FM}-x} - E_{\mathrm{FM}-z} - E_{\mathrm{stripy-AFM}-x}}{16},\\
A &= \frac{3E_{\mathrm{stripy-AFM}-x} - 3E_{\mathrm{stripy-AFM}-z} + E_{\mathrm{FM}-x} - E_{\mathrm{FM}-z}}{16},\\
D_{ij} &= \frac{E_{\mathrm{CW}} - E_{\mathrm{ACW}}}{12}.
\end{aligned}$$

Here, E_{CW} and E_{ACW} are the total energies of clockwise (90° ordered AFM-1) and anticlockwise (90° ordered AFM-2) spin configurations (see Fig. S5 [30]), respectively. J_1, J_2, A, λ, and D_{ij} are determined to be 1.34, 0.36, −0.46, −0.01, and 0.03 meV, respectively. It can be observed that the DMI in $WRuCl_6$ monolayer is weak, with D_{ij} being two orders of magnitude smaller than J_1. It therefore can be concluded that J_1 dominates the magnetic ground state, indicative of an in-plane collinear FM ground state for $WRuCl_6$ monolayer. In Fig. 4(b) of the MC simulation results, one can see that the Curie temperature is approximately 58 K, surpassing those of other bulk and 2D multiferroics, *e.g.*, bulk $AgCrO_2$ (21 K) [35], $MnRe_2O_8$ monolayer (31 K) [3], and CrI_3 monolayer (45 K) [24]. In accordance to the above Heisenberg spin Hamiltonian model, for symmetric P state, J_1, J_2, A, λ, and D_{ij} are 1.28, 0.35, −0.41, −0.02, and 0.03 meV, respectively. It correspondingly indicates a Curie temperature of approximately 55 K, as shown in Fig. S6(a) [30], which is comparable to that of asymmetric F_1 state (58 K). It should be noted that in the above model the magnetic exchange interactions J_{NN} and J'_{NN} are actually treated as J_1 (J_{NNN} and J'_{NNN} as J_2) due to the small interatom distance difference. In Fig. S7 [30], J_{NN}, J'_{NN}, J_{NNN}, and J'_{NNN} are defined. In case we consider the difference to include all the J_{NN}, J'_{NN}, J_{NNN}, and J'_{NNN}, a more explicit Heisenberg spin Hamiltonian model can be expressed as

$$\begin{aligned}
H = {} & H_0 - J_{\mathrm{NN}}\sum_{\langle ij\rangle}\boldsymbol{S}_i\boldsymbol{S}_j - J'_{\mathrm{NN}}\sum_{\langle ij'\rangle}\boldsymbol{S}_i\boldsymbol{S}_{j'} - J_{\mathrm{NNN}}\sum_{\langle mn\rangle}\boldsymbol{S}_m\boldsymbol{S}_n - J'_{\mathrm{NNN}}\sum_{\langle mn'\rangle}\boldsymbol{S}_m\boldsymbol{S}_{n'} - \lambda_{\mathrm{NN}}\sum_{\langle ij\rangle}\boldsymbol{S}_i^z\boldsymbol{S}_j^z - \lambda'_{\mathrm{NN}}\sum_{\langle ij'\rangle}\boldsymbol{S}_i^z\boldsymbol{S}_{j'}^z\\
& - A'\sum_i\left(\boldsymbol{S}_i^z\right)^2 - \sum_{\langle ij\rangle}\boldsymbol{D}_{ij}(\boldsymbol{S}_i\times\boldsymbol{S}_j),
\end{aligned}$$

where $\langle ij\rangle$ ($\langle ij'\rangle$) and $\langle mn\rangle$ ($\langle mn'\rangle$) stand for the magnetic atoms, and J_{NN}, J'_{NN}, J_{NNN}, and J'_{NNN} are the corresponding magnetic exchange interactions. In order to calculate these parameters accurately, FM, AFM–1, FiM–1, FiM–2, and FiM–3 states are taken into account; see Fig. S7 [30]. In Table S6 [30], the total energies for these orders are summarized, and results suggest that the in-plane FM order remains the magnetic ground state. In light of this, the magnetic interaction parameters J_{NN}, J'_{NN}, J_{NNN}, J'_{NNN}, λ_{NN}, λ'_{NN}, and A' can be determined by

$$\begin{aligned}
E_{\mathrm{FM}-x} &= E_0 - 16J_{\mathrm{NN}} - 8J'_{\mathrm{NN}} - 16J_{\mathrm{NNN}} - 8J'_{\mathrm{NNN}},\\
E_{\mathrm{FM}-z} &= E_0 - 16J_{\mathrm{NN}} - 8J'_{\mathrm{NN}} - 16J_{\mathrm{NNN}} - 8J'_{\mathrm{NNN}} - 16\lambda_{\mathrm{NN}} - 8\lambda'_{\mathrm{NN}} - 8A',\\
E_{\mathrm{AFM}-1-x} &= E_0 - 16J_{\mathrm{NN}} - 8J'_{\mathrm{NN}} - 8J_{\mathrm{NNN}} + 16J'_{\mathrm{NNN}},\\
E_{\mathrm{AFM}-1-z} &= E_0 - 16J_{\mathrm{NN}} - 8J'_{\mathrm{NN}} - 8J_{\mathrm{NNN}} + 16J'_{\mathrm{NNN}} - 16\lambda_{\mathrm{NN}} - 8\lambda'_{\mathrm{NN}} - 8A',\\
E_{\mathrm{FiM}-1-x} &= E_0 - 8J_{\mathrm{NN}} - 4J'_{\mathrm{NN}} - 4J_{\mathrm{NNN}} + 8J'_{\mathrm{NNN}},\\
E_{\mathrm{FiM}-1-z} &= E_0 - 8J_{\mathrm{NN}} - 4J'_{\mathrm{NN}} - 4J_{\mathrm{NNN}} + 8J'_{\mathrm{NNN}} - 8\lambda_{\mathrm{NN}} - 4\lambda'_{\mathrm{NN}} - 8A',\\
E_{\mathrm{FiM}-2-x} &= E_0 - 8J_{\mathrm{NN}} - 4J'_{\mathrm{NN}} - 4J_{\mathrm{NNN}} - 8J'_{\mathrm{NNN}},\\
E_{\mathrm{FiM}-2-z} &= E_0 - 8J_{\mathrm{NN}} - 4J'_{\mathrm{NN}} - 4J_{\mathrm{NNN}} - 8J'_{\mathrm{NNN}} - 8\lambda_{\mathrm{NN}} - 4\lambda'_{\mathrm{NN}} - 8A',
\end{aligned}$$

$$
\begin{aligned}
E_{\text{FiM}-3-x} &= E_0 - 8J'_{\text{NN}},\\
E_{\text{FiM}-3-z} &= E_0 - 8J'_{\text{NN}} - 8\lambda'_{\text{NN}} - 8A',\\
J_{\text{NN}} &= \frac{2E_{\text{FiM}-3-x} + 2E_{\text{FM}-x} - 4E_{\text{AFM}-1-x} - 5E_{\text{FiM}-2-x} + 5E_{\text{FiM}-1-x}}{32},\\
J'_{\text{NN}} &= \frac{2E_{\text{FiM}-1-x} - E_{\text{AFM}-1-x} - E_{\text{FiM}-3-x}}{8},\\
J_{\text{NNN}} &= \frac{2E_{\text{AFM}-1-x} - 2E_{\text{FM}-x} - 3E_{\text{FiM}-1-x} + 3E_{\text{FiM}-2-x}}{16},\\
J'_{\text{NNN}} &= \frac{\text{E}_{\text{FiM}-1-x} - \text{E}_{\text{FiM}-2-x}}{16},\\
\lambda_{\text{NN}} &= \frac{E_{\text{FiM}-3-z} - E_{\text{FiM}-3-x} + E_{\text{FM}-x} - E_{\text{FM}-z}}{16},\\
\lambda'_{\text{NN}} &= \frac{2E_{\text{AFM}-1-x} - 2E_{\text{FiM}-1-x} + E_{\text{FiM}-3-x} - E_{\text{FM}-x}}{8} + \frac{E_{\text{FM}-z} + E_{\text{FiM}-1-z} - E_{\text{FiM}-3-z} - 2E_{\text{AFM}-1-z}}{8},\\
A' &= \frac{2E_{\text{FiM}-1-x} + E_{\text{FM}-x} - 2E_{\text{AFM}-1-x}}{8},\\
&\quad + \frac{2E_{\text{AFM}-1-z} - E_{\text{FM}-z} - E_{\text{FiM}-1-z}}{8}.
\end{aligned}
$$

In particular, J_{NN}, J'_{NN}, J_{NNN}, J'_{NNN}, λ_{NN}, λ'_{NN}, and A' are 1.42, 1.22, 0.49, 0.48, −0.08, −0.55, and −0.50 meV, respectively. It therefore is an indication that the $WRuCl_6$ monolayer (F_1 state) exhibits an in-plane collinear FM ground state with a Curie temperature of 62 K; see Fig. S6(b) [30], which is comparable to that attained from the simple model (58 K). It should be pointed out that the operational temperature for using the FM order as a storage parameter must be below the Curie temperature. In Tables S4–S8 [30], the total energies of $WRuCl_6$ monolayer with different magnetic states are provided, considering different U_{eff} values. It can be seen that the in-plane collinear FM state remains the magnetic ground state with different U_{eff} values. It is obvious that furthermore, the easy-magnetization axis of the F_1 state is consistently along the [–110]/[1–10] direction; see Figs. S8–S10 [30]. It therefore can be concluded that the magnetic properties of $WRuCl_6$ monolayer are stable against the variation of U_{eff}.

In Figs. 3 and 5, PDOS and band structure of $WRuCl_6$ monolayer are shown, respectively. It can be observed that $WRuCl_6$ monolayer is characterized as a semiconductor with a band gap of 0.57 eV, with the valence-band maximum (VBM) and conduction-minimum (CBM) being primarily contributed by W $5d$ orbitals. It is of importance that states near the Fermi level reveal 100% spin polarization, that is, VBM and CBM are, respectively, located within the spin-up and spin-down channel. This indicates that $WRuCl_6$ monolayer is an intrinsic bipolar magnetic semiconductor [36,37]; thus, the unique half metallicity and spin-polarized carriers can be attained by adjusting the position of the Fermi level. In particular, electron doping by applying a negative electric gate can shift the Fermi level upward, causing CBM to fall below the Fermi level and giving rise to charge carriers with spin-down polarization. In an alternative way, a positive electric gate induces hole doping, moving the Fermi level down and making VBM above the Fermi level; therefore, the spin polarization of the charge carriers is fixed to be spin up. In other words, the spin polarization of charge carriers can be switched by reversing the polarity of the electric gate.

Depending on the bonding direction of the metal dimer, three energetically equivalent FE states arise, i.e., F_1, F_2 [Fig. 2(c)] and F_3 [Fig. 2(e)]. It is highly interesting that the direction of the easy-magnetization axis in F_2 and F_3 states is also along with the bonding direction of the metal dimer; see Figs. 2(d) and 2(f). Such an interlocking between the ferromagnetism and ferroelectricity conforms to the mechanism. Based on the Berry phase method [38], the spontaneous

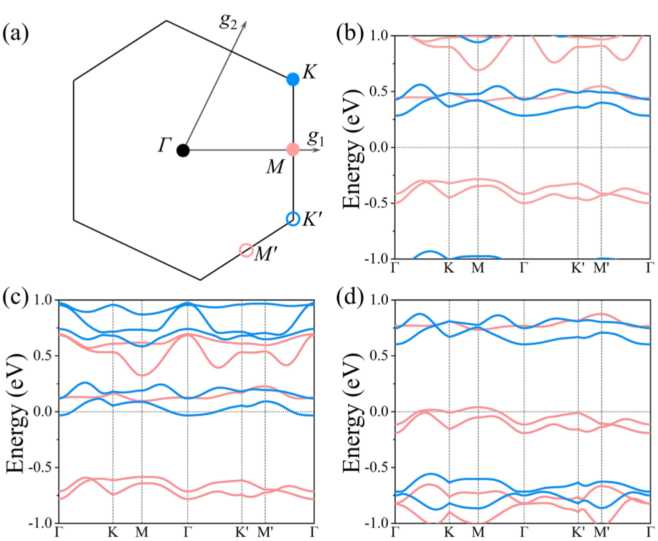

FIG. 5. (a) Two-dimensional Brillouin zone of $WRuCl_6$ monolayer of F_1 states. Γ (0.00, 0.00), K (0.35, 0.35), M (0.50, 0.00), K' (0.65, −0.35), and M'(0.50, −0.50) points are denoted. Spin-polarized band structure of FM $WRuCl_6$ monolayer (b) without doping, (c) doped with 0.3 electrons, and (d) doped with 0.3 holes, respectively. The Fermi level is set to zero.

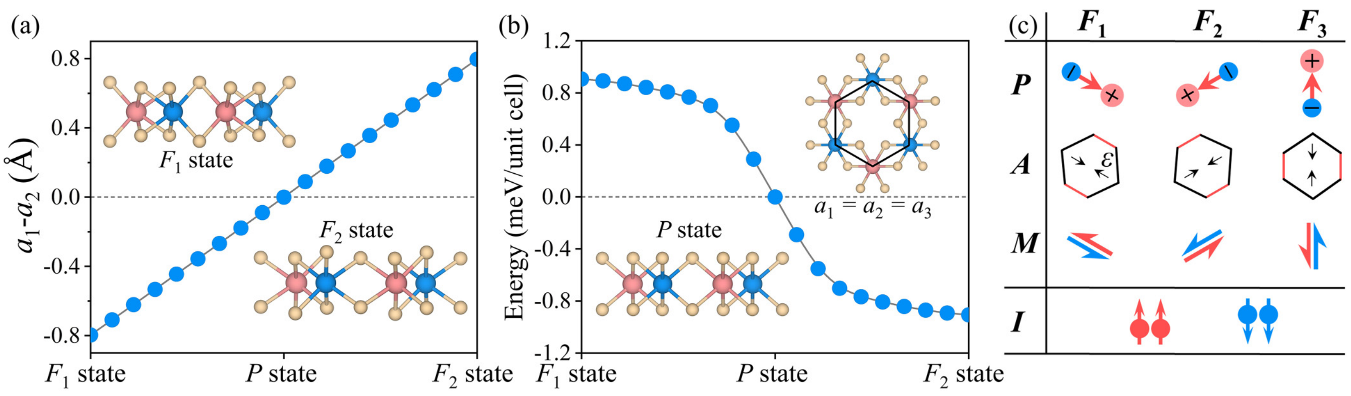

FIG. 6. Variation of (a) $a_1 - a_2$, and (b) energy difference ΔE of $WRuCl_6$ monolayer for F_1-to-F_2 phase transition. (c) Possible storage signals in multifunctional triferroic $WRuCl_6$ monolayer. P, A, and M correspond to the FE, FA, and FM orders, respectively, and I stands for spin-polarized carrier. Each state has two energetically degenerate FM ground states with opposite spin direction, indicated by red and blue arrows.

in-plane electric polarization of all three states is 1.89×10^2 pC/m, pointing towards [1–10], [–2–10], and [120] directions for F_1, F_2, and F_3 states, respectively. The electric polarization is substantially larger than other 2D FE materials such as H'-Co_2CF_2 (11.7 pC/m) [39] and $AgBiP_2Se_6$ monolayer (4.3 pC/m) [40], and comparable to that of $FeHfSe_3$ monolayer (1.29×10^2 pC/m) [41]. This indicates the feasibility of experimental detection.

In order to evaluate the stability of the ferroelectricity and the feasibility of electric polarization switching, climbing image nudged elastic band (CINEB) method is used to determine the switching pathway and corresponding energy barrier [19]. Taking the FE phase transition from F_1 to F_2 state as a representative, the minimum-energy pathway of the FE switching is shown in Fig. 4(c). Obviously, the transition state is the P state (D_3-point symmetry) with $a_1 = a_2 = a_3 = 3.34$ Å. The energy barrier along this pathway is 0.31 eV per unit cell, larger than that of In_2Se_3 monolayer (0.07 eV per unit cell) [42], while comparable to or even smaller than those of H'-Co_2CF_2 monolayer (0.20 eV per unit cell) [39] and $Cr(TDZ)_2$ monolayer (0.37 eV per unit cell) [1]. The moderate energy barrier ensures an easy FE switching as well as a stable FE order. In Fig. S11 [30], the variation of the electric polarization of $WRuCl_6$ monolayer from F_1 to F_2 state is illustrated. In order to verify the effect of an external electric field on the FE phase transition, as a representative, an x-direction ([100]) field is applied to F_1 and F_2 states that have numerically equal but opposite x-direction components of electric polarization. In Fig. 4(d), the variation of the total energy difference between F_1 and F_2 states $\Delta E = E_{F_1} - E_{F_2}$ with respect to the electric field is shown. It is evident that the electric field can lift the degeneracy of two FE states and stabilize one of them; for example, ΔE reaches $-0.52(0.52)$ eV per unit cell under a field of $0.2(-0.2)$ V/Å and F_1 (F_2) phase is more stable than the F_2 (F_1) counterpart. In addition, the phase transition of the ferroelastic $WRuCl_6$ monolayer could probably be induced by gluing it onto a flexible substrate to apply an external stress by such as epitaxy, thermal-expansion mismatch, and directly stretching, compressing or bending the substrate [43], similar as that experimentally verified in ferroelastic β'-In_2Se_3 of 120° rotation symmetry [44].

Interestingly, three FE states of $WRuCl_6$ monolayer correspond also to three FA orientation variants, due to the three equivalent directions for structural distortion in P state. The FA phase transition can be immediately illustrated by the variation of a_1, a_2, and a_3. Similar to T'-phase MX_2 monolayer [29], the relative thermodynamic stability between different FA states can be switched by applying appropriate mechanical stress to achieve stress-controlled phase transition. The coupling between FA and FE orders indicates the potential of electrically controlled ferroelasticity. In Fig. 6(a), taking the switching process from F_1 to F_2 state as an example, the variation in $(a_1 - a_2)$ is presented. It is obvious that the FA phase transition follows the FE switching, and the interlocked ferroelasticity and ferroelectricity ensures the fascinating electrically controlled ferroelasticity.

In order to reveal the stability of the magnetic order in each polarized state, we refer to the energy difference $\Delta E = E_{[-2-10]} - E_{[1-10]}$, where $E_{[-2-10]}$ and $E_{[1-10]}$ are the total energies of the states with the spin ordering along [–2–10] and [1–10] directions, respectively. It immediately shows the switching of the easy-magnetization axis during the phase transition from F_1 to F_2 state, as indicated in Fig. 6(b). As mentioned above, the FM state is also switched simultaneously during this process, and the spin direction of the magnetic ground state is aligned parallel/antiparallel to the direction of electric polarization. In other words, the aspirational electrically controlled magnetism can also be achieved in $WRuCl_6$ monolayer.

In practice, $WRuCl_6$ monolayer with robust multiferroic coupling allows the switchable ferroic states through external electric field. It is of interest that as shown in Fig. 6(c), $WRuCl_6$ monolayer not only has FE/FA/FM order, but also exhibits an extra storage parameter, i.e., the spin-polarized carrier (I_1 and I_2). It should be pointed out that the strong coupling between FE/FA/FM order seemingly cannot improve the storage capacity, only if external fields can be applied to switch the storage states. In case of $WRuCl_6$ monolayer with greater flexibility compared to traditional ferroic materials, interestingly, different external fields (electric field, strain, and magnetic field) can be applied to cause the switch of a certain ferroic parameter. In particular, for the material each FE/FA state corresponds to two reversible storage orders, i.e., the spin order (parallel or antiparallel to the electric polarization) and spin-polarized carrier (electron or hole doping), which can be considered as effective signals to enhance the storage capacity. In experiments, such two storage orders could be characterized using MicbiaoroSense vibrating sample magnetometer and spin-polarized tunneling measurement [45,46], and can be switched by external magnetic field and the gate voltage [24,47], respectively. In this view, therefore, the coexistence of multiferroic coupling and multiple storage states can probably be realized in $WRuCl_6$ monolayer.

IV. CONCLUSIONS

In summary, we demonstrate that nonvolatile electrically controlled ferromagnetism and ferroelasticity and multistate storage can be realized in $WRuCl_6$ monolayer. In regard to $WRuCl_6$ monolayer, it not only has spontaneous in-plane electric polarization, but also shows an FM ground state with the direction of the easy-magnetization axis aligned parallel/antiparallel to electric polarization. In addition, the ferroelasticity and ferroelectricity in $WRuCl_6$ monolayer are interlocked, ensuring also the realization of electrically controlled ferroelasticity. Our work broadens the exploration of multiferroic coupling physics, and provides a perspective in the fields of spintronics and multistate storage, expecting to draw attention from experiments.

ACKNOWLEDGMENT

This work is financially supported by the National Natural Science Foundation of China (Grants No. 52272223 and No. 12074217).

[1] X. Li, Q.-B. Liu, Y. Tang, W. Li, N. Ding, Z. Liu, H.-H. Fu, S. Dong, X. Li, and J. Yang, Quintuple function integration in two-dimensional Cr(II) five-membered heterocyclic metal organic frameworks via tuning ligand spin and lattice symmetry, J. Am. Chem. Soc. **145**, 7869 (2023).

[2] C. Lu, M. Wu, L. Lin, and J. M. Liu, Single-phase multiferroics: New materials, phenomena, and physics, Natl. Sci. Rev. **6**, 653 (2019).

[3] S. Yu, Y. Xu, Y. Dai, D. Sun, B. Huang, and W. Wei, Spin spiral order induced ferroelectricity in $MnRe_2O_8$ monolayer, Phys. Rev. B **108**, 174429 (2023).

[4] J. J. Zhang, L. Lin, Y. Zhang, M. Wu, B. I. Yakobson, and S. Dong, Type-II multiferroic $Hf_2VC_2F_2$ MXene monolayer with high transition temperature, J. Am. Chem. Soc. **140**, 9768 (2018).

[5] X. Xuan, W. Guo, and Z. Zhang, Ferroelasticity in two-dimensional tetragonal materials, Phys. Rev. Lett. **129**, 047602 (2022).

[6] W. Eerenstein, N. D. Mathur, and J. F. Scott, Multiferroic and magnetoelectric materials, Nature (London) **442**, 759 (2006).

[7] Y. Gao, M. Wu, and P. Jena, A family of ionic supersalts with covalent-like directionality and unconventional multiferroicity, Nat. Commun. **12**, 1331 (2021).

[8] W.-R. Geng, Y.-L. Tang, Y.-L. Zhu, Y.-J. Wang, B. Wu, L.-X. Yang, Y.-P. Feng, M.-J. Zou, T.-T. Shi, Y. Cao, and X.-L. Ma, Magneto–electric–optical coupling in multiferroic $BiFeO_3$-based films, Adv. Mater. **34**, 2106396 (2022).

[9] S. Shen, X. Xu, B. Huang, L. Kou, Y. Dai, and Y. Ma, Intrinsic triferroicity in a two-dimensional lattice, Phys. Rev. B **103**, 144101 (2021).

[10] L. Yang, Y. Gao, M. Wu, and P. Jena, Interfacial triferroicity in monolayer chromium dihalide, Phys. Rev. B **105**, 094101 (2022).

[11] C. Tang, L. Zhang, S. Sanvito, and A. Du, Enabling room-temperature triferroic coupling in dual transition-metal dichalcogenide monolayers via electronic asymmetry, J. Am. Chem. Soc. **145**, 2485 (2023).

[12] G. G. Kresse and J. J. Furthmüller, Efficient iterative schemes for ab initio total-energy calculations using a plane-wave basis set, Phys. Rev. B **54**, 11169 (1996).

[13] G. Kresse and D. Joubert, From ultrasoft pseudopotentials to the projector augmented-wave method, Phys. Rev. B **59**, 1758 (1999).

[14] J. P. Perdew, K. Burke, and M. Ernzerhof, Generalized gradient approximation made simple, Phys. Rev. Lett. **77**, 3865 (1996).

[15] S. L. Dudarev, G. A. Botton, S. Y. Savrasov, C. J. Humphreys, and A. P. Sutton, Electron-energy-loss spectra and the structural stability of nickel oxide: An LSDA+U study, Phys. Rev. B **57**, 1505 (1998).

[16] M. Xu, C. Huang, Y. Li, S. Liu, X. Zhong, P. Jena, E. Kan, and Y. Wang, Electrical control of magnetic phase transition in a type-I multiferroic double-metal trihalide monolayer, Phys. Rev. Lett. **124**, 067602 (2020).

[17] H. J. Monkhorst and J. D. Pack, Special points for Brillouin-zone integrations, Phys. Rev. B **13**, 5188 (1976).

[18] A. Togo and I. Tanaka, First principles phonon calculations in materials science, Scr. Mater. **108**, 1 (2015).

[19] D. Sheppard, P. Xiao, W. Chemelewski, D. D. Johnson, and G. Henkelman, A generalized solid-state nudged elastic band method, J. Chem. Phys. **136**, 074103 (2012).

[20] C. Huang, J. Feng, J. Zhou, H. Xiang, K. Deng, and E. Kan, Ultra-high-temperature ferromagnetism in intrinsic tetrahedral semiconductors, J. Am. Chem. Soc. **141**, 12413 (2019).

[21] S. Chib and E. Greenberg, Understanding the metropolis-hastings algorithm, Am. Stat. **49**, 327 (1995).

[22] M. Newman and G. T. Barkema, *Monte Carlo Methods in Statistical Physics* (Oxford University Press, Oxford, UK, 1999).

[23] L. Liu, X. Ren, J. Xie, B. Cheng, W. Liu, T. An, H. Qin, and J. Hu, Magnetic switches via electric field in BN nanoribbons, Appl. Surf. Sci. **480**, 300 (2019).

[24] B. Huang, G. Clark, E. Navarro-Moratalla, D. R. Klein, R. Cheng, K. L. Seyler, D. Zhong, E. Schmidgall, M. A. McGuire, D. H. Cobden, W. Yao, D. Xiao, P. JarilloHerrero, and X. Xu, Layer-dependent ferromagnetism in a van der Waals crystal down to the monolayer limit, Nature (London) **546**, 270 (2017).

[25] L. N. Kapoor, S. Mandal, P. C. Adak, M. Patankar, S. Manni, A. Thamizhavel, and M. M. Deshmukh, Observation of standing spin waves in a van der Waals magnetic material, Adv. Mater. **33**, 2005105 (2021).

[26] Y. Yekta, H. Hadipour, E. Şaşıoğlu, C. Friedrich, S. A. Jafari, S. Blügel, and I. Mertig, Strength of effective Coulomb interaction in two-dimensional transition-metal halides MX_2 and MX_3 (M = Ti, V, Cr, Mn, Fe, Co, Ni; X = Cl, Br, I), Phys. Rev. Mater. **5**, 034001 (2021).

[27] Q. Sun and N. Kioussis, Prediction of manganese trihalides as two-dimensional Dirac half-metals, Phys. Rev. B **97**, 094408 (2018).

[28] K. Yang, F. Fan, H. Wang, D. I. Khomskii, and H. Wu, VI_3: A two-dimensional Ising ferromagnet, Phys. Rev. B **101**, 100402(R) (2020).

[29] W. Li and J. Li, Ferroelasticity and domain physics in two-dimensional transition metal dichalcogenide monolayers, Nat. Commun. **7**, 10843 (2016).

[30] See Supplemental Material at http://link.aps.org/supplemental/10.1103/PhysRevB.110.064417 for (i) cohesive energy, elastic constants, AIMD results, phonon dispersion spectrum of monolayer (in F1 state); (ii) total energies for monolayer (in F1 state) and / heterobilayer with different magnetic orderings; (iii) total energies for monolayer with different magnetic orderings under different values; (iv) spin charge density, orbital energy splitting of metal atoms, PDOS, band structure, Curie temperature and possible magnetic states of monolayer (for F1 state); (v) local magnetic moment and MAE of monolayer (for F1 state) under different values; (vi) electric polarization of monolayer for F1-to-F2 phase transition.

[31] M.-H. Whangbo, H. Xiang, H.-J. Koo, E. E. Gordon, and J. L. Whitten, Electronic and structural factors controlling the spin orientations of magnetic ions, Inorg. Chem. **58**, 11854 (2019).

[32] M.-H. Whangbo, E. E. Gordon, H. Xiang, H.-J. Koo, and C. Lee, Prediction of spin orientations in terms of HOMO–LUMO interactions using spin–orbit coupling as perturbation, Acc. Chem. Res. **48**, 3080 (2015).

[33] N. D. Mermin and H. Wagner, Absence of ferromagnetism or antiferromagnetism in one- or two-dimensional isotropic Heisenberg models, Phys. Rev. Lett. **17**, 1133 (1966).

[34] J. M. Kosterlitz, The critical properties of the two-dimensional xy model, J. Phys. C: Solid State Phys. **7**, 1046 (1974).

[35] S. Seki, Y. Onose, and Y. Tokura, Spin-driven ferroelectricity in triangular lattice antiferromagnets $ACrO_2$ (A = Cu, Ag, Li, Na), Phys. Rev. Lett. **101**, 067204 (2008).

[36] N. Luo, C. Si, and W. Duan, Structural and electronic phase transitions in ferromagnetic monolayer VS_2 induced by charge doping, Phys. Rev. B **95**, 205432 (2017).

[37] H.-X. Cheng, J. Zhou, W. Ji, Y.-N. Zhang, and Y.-P. Feng, Two-dimensional intrinsic ferrovalley GdI_2 with large valley polarization, Phys. Rev. B **103**, 125121 (2021).

[38] R. D. King-Smith and D. Vanderbilt, Theory of polarization of crystalline solids, Phys. Rev. B **47**, 1651 (1993).

[39] C. Huang, J. Zhou, H. Sun, F. Wu, Y. Hou, and E. Kan, Toward room-temperature electrical control of magnetic order in multiferroic van der Waals materials, Nano Lett. **22**, 5191 (2022).

[40] H. Liu, S. Yu, Y. Wang, B. Huang, Y. Dai, and W. Wei, Excited-state properties of $CuInP_2S_6$ monolayer as photocatalyst for water splitting, J. Phys. Chem. Lett. **13**, 1972 (2022).

[41] S. Yu, Y. Wang, S. Wang, H. Zhang, Ba. Huang, Y. Dai, and W. Wei, Robust intrinsic multiferroicity in a $FeHfSe_3$ layer, J. Phys. Chem. Lett. **12**, 8882 (2020).

[42] W. Ding, J. Zhu, Z. Wang, Y. Gao, D. Xiao, Y. Gu, Z. Zhang, and W. Zhu, Prediction of intrinsic two-dimensional ferroelectrics in In_2Se_3 and other III_2-VI_3 van der Waals materials, Nat. Commun. **8**, 14956 (2017).

[43] Z. Dai, L. Liu, and Z. Zhang, Strain engineering of 2D materials: Issues and opportunities at the interface, Adv. Mater. **31**, 1805417 (2019).

[44] C. Xu, J. Mao, X. Guo, S. Yan, Y. Chen, T. W. Lo, C. Chen, D. Lei, X. Luo, J. Hao, C. Zheng, and Y. Zhu, Two-dimensional ferroelasticity in van der Waals β'-In_2Se_3, Nat. Commun. **12**, 3665 (2021).

[45] P. Perlepe, I. Oyarzabal, A. Mailman, M. Yquel, M. Platunov, I. Dovgaliuk, M. Rouzieres, P. Negrier, D. Mondieig, E. A. Suturina, M.-A. Dourges, S. Bonhommeau, R. A. Musgrave, K. S. Pedersen, D. Chernyshov, F. Wilhelm, A. Rogalev, C. Mathoniere, and R. Clerac, Metal-organic magnets with large coercivity and ordering temperatures up to 242 °C, Science **370**, 587 (2020).

[46] P. M. Tedrow and R. Meservey, Spin-dependent tunneling into ferromagnetic nickel, Phys. Rev. Lett. **26**, 192 (1971).

[47] S. J. Gong, C. Gong, Y. Y. Sun, W. Y. Tong, C. G. Duan, J. H. Chu, and X. Zhang, Electrically induced 2D half-metallic antiferromagnets and spin field effect transistors, Proc. Natl. Acad. Sci. USA **115**, 8511 (2018).